Superconducting phase of Ti_xO_y thin films grown by molecular beam epitaxy

Yasemin Ozbek,[1] Cooper Brooks,[1] Xuanyi Zhang,[1] Athby Al-Tawhid,[1] Vladmir A. Stoica,[2]
Zhan Zhang,[3] and Divine P. Kumah[1,*]
[1]*Department of Physics, North Carolina State University, Raleigh, North Carolina 27695, USA*
[2]*Department of Materials Science and Engineering and Materials Research Institute, Pennsylvania State University, University Park, Pennsylvania 16802, USA*
[3]*Advanced Photon Source, Lemont, Illinois 60439, USA*

(Received 2 March 2022; accepted 8 June 2022; published 27 June 2022; corrected 28 November 2022)

We investigate the complex relationship between the growth conditions and the structural and transport properties of Ti_xO_y thin films grown by molecular beam epitaxy. Transport properties ranging from metallicity to superconductivity and insulating states are stabilized by effectively tuning the O/Ti ratio via the Ti flux rate and the O partial pressure P_{Ox} for films grown on (0001)-Al_2O_3 substrates at 850° C. A cubic c-$TiO_{1\pm\delta}$ buffer layer is formed for low O/Ti ratios, while a corundum cr-Ti_2O_3 layer is formed under higher-oxidizing conditions. Metallicity is observed for c-$TiO_{1-\delta}$ buffer layers. The superconducting γ-Ti_3O_5 Magnéli phase is found to nucleate on a c-$TiO_{1-\delta}$ buffer for intermediate P_{Ox} conditions, and an insulator-superconducting transition is observed at 4.5 K ($T_C^{\text{onset}} = 6K$) for 85 nm thick films. Strain relaxation of γ-Ti_3O_5 occurs with increasing film thickness and correlates with a thickness-dependent increase in T_C observed for Ti_xO_y thin films.

DOI: 10.1103/PhysRevMaterials.6.064805

I. INTRODUCTION

The simple binary oxide titanium oxide, Ti_xO_y, forms a wide range of polymorphs and Magnéli (Ti_nO_{n-1}) phases with properties ranging from insulating rutile and anatase TiO_2 to corundum cr-Ti_2O_3, which undergoes a metal-insulator transition at 450 K, to superconducting cubic NaCl-type c-TiO (bulk $T_C = 1$–2 K) [1–5]. The ability to utilize the epitaxial stabilization of a given phase in thin films synthesized with atomic-layer control provides a route to tune the electronic properties of Ti_xO_y [6–12]. Recent reports of superconductivity in Ti_xO_y thin films as high as 11 K have sparked renewed interest in superconducting binary oxides [13]. The transition temperature T_c has been reported to depend on the film thickness [14,15], oxygen stoichiometry [16,17], and growth temperature [15]. The enhanced T_C in thin films was attributed to the formation of a high-growth-temperature orthorhombic o-Ti_2O_3 phase[15] ($T_C = 8$ K), excess oxygen in c-$TiO_{1+\delta}$ films ($T_C = 7.4$ K) [6,16], interfacial superconductivity at stoichiometric c-TiO/nonstoichiometric $TiO_{1+\delta}$ interfaces in core-shell structures ($T_C = 11$ K) [13], and the epitaxial stabilization of the γ-Ti_3O_5 ($T_C = 7$ K) [18] Magnéli phase. Studies of mixed eutectic phases indicated a correlation between the coexistence of c-$TiO_{1+\delta}$, cr-Ti_2O_3, and γ-Ti_3O_5 phases with enhanced T_c, hinting at the nontrivial role of interactions at interfaces between Ti_xO_y phases in enhancing T_C [19]. Thus, a critical step in understanding the enhanced transition temperature T_c in Ti_xO_y thin films involves elucidating the atomic-scale structure and composition of the system as a function of growth conditions (growth temperature, oxygen pressure, film thickness) using synthesis techniques which allow for the control of the film stoichiometry.

The relation between the transport properties and structural phases of Ti_xO_y was previously investigated for thin films grown by pulsed laser deposition (PLD) and molecular beam epitaxy (MBE) on (0001)-oriented α-Al_2O_3 [6,11,16,18–22]. Figure 1 shows the lattice structures of the lattice planes of Ti_xO_y phases grown epitaxially on (0001)-oriented α-Al_2O_3. A summary of reported phases and their superconducting T_C is given in Table I. Li *et al.* reported an orthorhombic o-Ti_2O_3 phase for films grown by PLD above 650 °C as evidenced by high-resolution transmission electron microscopy (TEM), Raman spectroscopy, and specular x-ray diffraction measurements (XRD) [11,15]. They observed a dependence of T_c on the film thickness of the o-Ti_2O_3 phase with a maximum T_c of 8 K for 168 nm thick films [15]. Low-temperature growth (below 650 °C) led to the stabilization of the insulating bulk trigonal cr-Ti_2O_3 phase. Fan *et al.* investigated the growth oxygen pressure dependence between 4.5×10^{-6} and 6.7×10^{-6} Torr for 80 nm thick films and found a suppression of superconductivity at high oxygen growth pressures [16]. The conclusion of a c-TiO structure was based on the analysis of the film layers close to the substrate by TEM and XRD measurements [6]. It is important to note that while multiple structures have been proposed and/or observed, T_C are consistent with the reported thickness dependence [14,15]. Additionally, local TEM measurements indicated a transitional c-TiO interface layer for o-Ti_2O_3 [15]. A study of eutectic Ti_xO_y prepared by varying the growth and postgrowth Ar annealing conditions showed a variation of T_c with the relative fractions of c-TiO, γ-Ti_3O_5, and cr-Ti_2O_3. Thus, the complexity of the system requires a systematic investigation of how specific growth conditions influence the relative fractions of the phases of Ti_xO_y and the resulting effect on

---

[*] dpkumah@ncsu.edu

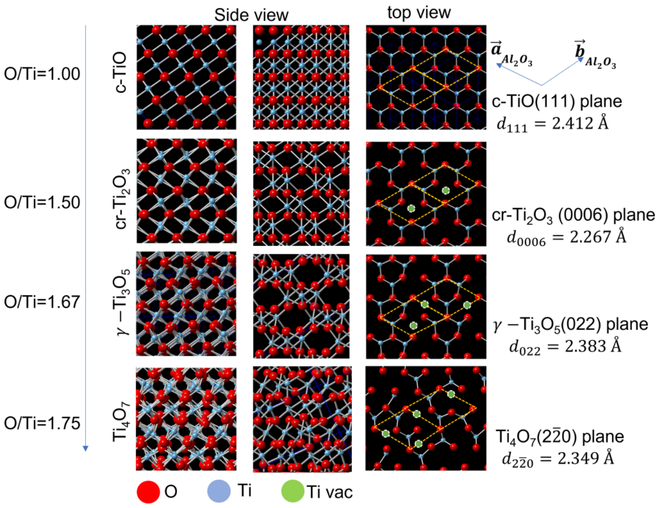

FIG. 1. Atomic structure of cubic *c*-TiO, corundum cr-Ti$_2$O$_3$, γ-Ti$_3$O$_5$, and Ti$_4$O$_7$ along projections in the α-Al$_2$O$_3$ [10$\bar{1}$0] direction (left panel), the [11$\bar{2}$0] direction (middle panel), and the [0001] direction (right panel).

the transport properties. In this paper, we investigate the transport and structural properties of Ti$_x$O$_y$ films grown by MBE to elucidate the effect of tuning the film stoichiometry and thickness on the superconducting properties of Ti$_x$O$_y$ thin films. Here, we perform high-resolution synchrotron x-ray diffraction measurements on Ti$_x$O$_y$ films grown on (0001)-oriented α-Al$_2$O$_3$ at 850 °C. The film stoichiometry is tuned by controlling the growth oxygen pressure $P_{\rm Ox}$, Ti flux rate, and film thickness. $P_{\rm Ox}$ is varied from 4×10^{-8} to 1×10^{-6} Torr. Films grown at low-oxygen partial pressures ($P_{\rm Ox} \leqslant 1 \times 10^{-7}$ Torr) are found to be metallic with carrier concentrations ranging from 3×10^{22} cm^{-3} at 300 K to 6×10^{21} cm^{-3} at 10 K. Metallicity is correlated with the formation of oxygen-deficient *c*-TiO$_{1-\delta}$. By tuning $P_{\rm Ox}$, the Ti flux rate, and the film thickness, an insulating-superconducting transition is observed in 85 nm thick films, which are characterized by a thin *c*-TiO$_{1\pm\delta}$ interfacial buffer layer and the formation of the γ-Ti$_3$O$_5$ phase. Strain relaxation is observed in γ-Ti$_3$O$_5$ with increasing film thickness and correlates with a thickness-tuned T_c observed in Ti$_x$O$_y$ films [14,15].

TABLE I. Summary of reported Ti$_x$O$_y$ structures and superconducting transition temperatures T_c. I refers to the insulating phase.

Substrate (Method)	Thickness	Structure	T_c
Al$_2$O$_3$ (PLD)	80 nm	TiO$_{1\pm\delta}$	7.4 K [6]
(Sintering)	bulk	TiO$_{1\pm\delta}$	5.5 K [22]
Al$_2$O$_3$(PLD)	168 nm	*o*-Ti$_2$O$_3$	8 K [15]
Al$_2$O$_3$(PLD)	120 nm	*o*-Ti$_2$O$_3$	I (no T_c) [11]
Al$_2$O$_3$ (PLD)	120 nm	γ-Ti$_3$O$_5$	7.1 [18]
LSAT, MgAl$_2$O$_4$ (PLD)	120 nm	Ti$_4$O$_7$	3.0 [18]
Al$_2$O$_3$ (PLD)	80 nm	TiO$_{1\pm\delta}$	1.4-6 K [16]
Al$_2$O$_3$ (PLD)	150 nm	cr-Ti$_2$O$_3$	I(no T_c) [20]

II. RESULTS AND DISCUSSION

Ti$_x$O$_y$ films with thicknesses of 25–85 nm were grown by oxide MBE. Prior to growth, the Al$_2$O$_3$ substrates were annealed at 1100 °C in a tube furnace tube for 12 h. Atomic force microscope images show smooth surfaces with atomic steps. The films were grown by deposition of Ti from an effusion cell under partial pressures of molecular oxygen ranging from 4×10^{-8} to 1×10^{-6} Torr at a substrate temperature of 850 °C. The growth rates were determined from the Ti fluxes measured by a quartz crystal monitor and x-ray reflectivity measurements to be 1.3–2.5 Å/min. The sample growth conditions are summarized in Table II. After growth, the films were cooled down at a rate of 25 °C/min from the deposition temperature to room temperature in vacuum.

Figure 2(a) shows an *in situ* reflection high-energy electron diffraction (RHEED) image of the initial Al$_2$O$_3$ substrate surface prior to deposition of the Ti$_x$O$_y$ films at $P_{\rm Ox} = 2 \times 10^{-7}$ Torr. Figure 2(b) shows the RHEED pattern after the deposition of 1 monolayer (ML) of Ti$_x$O$_y$. Roughening and relaxation are evident from the spotty nature of the RHEED pattern and the development of streaks with a closer spacing than the diffraction from the substrate. A streaky two-dimensional (2D) pattern emerges after the second ML and remains for the entire film growth. Figures 2(c) and 2(d) show the RHEED patterns after the growth of an 85 nm thick film along the [11$\bar{2}$0] and [10$\bar{1}$0] directions, respectively. The narrow streaks are indicative of a smooth 2D surface. Along the [10$\bar{1}$0] direction, a 3*x* reconstruction is observed. A comparison of the final RHEED patterns of samples A–F is shown in Fig. S1 in the Supplemental Material [23]. Atomic force microscope images of the as-grown films (see Fig. S2 in the Supplemental Material) [23] show atomically flat layers with steplike features identical to the substrate.

A. Transport properties

The dependence of the transport properties on the film thickness and growth conditions is determined by comparing the resistivities of a series of Ti$_x$O$_y$ films with thicknesses between 25 and 85 nm for $4 \times 10^{-8} \leqslant P_{\rm Ox} \leqslant 3 \times 10^{-7}$ Torr in Fig. 3(a). The transport measurements are performed in the van der Pauw configuration using Au contacts deposited on the corners of 5 × 5 mm^2 samples. Films grown with $P_{\rm Ox} \leqslant 1 \times 10^{-7}$ Torr are metallic for thicknesses less than 45 nm. Growth at higher oxygen pressures ($P_{\rm Ox} \geqslant 3 \times 10^{-7}$ Torr) results in insulating transport properties.

At the intermediate growth pressure of $P_{\rm Ox} = 2 \times 10^{-7}$ Torr, the transport properties depend on the film thickness and the Ti flux rate. The 45 nm film grown at $P_{\rm Ox} = 2 \times 10^{-7}$ Torr (sample D) is metallic and undergoes a metal-superconducting transition at ∼3.7 K. The thicker 85 nm film (sample E) is insulating below 300 K and transitions to a superconducting state at 4.5 K. The absence of superconductivity above 2 K for the 25 nm thick films, for the Ti flux rates investigated, is consistent with the thickness dependence of T_c observed for PLD grown films [15]. Films grown with $P_{\rm Ox} > 8 \times 10^{-7}$ Torr are insulating due to the formation of TiO$_2$, as evidenced by x-ray diffraction measurements.

Superconductivity in the 85 nm film (sample E) is confirmed by measuring the resistance as a function of a magnetic

TABLE II. Summary of growth conditions, film thickness, and measured phases and transport properties of MBE-grown $\mathrm{Ti}_x\mathrm{O}_y$ films on (0001)-oriented α-$\mathrm{Al_2O_3}$. I, M, and SC refer to the insulating, metallic, and superconducting phases, respectively. $P_{\mathrm{Ox}}/\mathrm{Ti}_{\mathrm{rate}}$ are normalized to the values for the superconducting sample E.

Sample	Thickness (nm)	Ti flux rate (atoms/cm^2 s)	$\mathrm{P_{Ox}}$ (Torr)	Normalized $P_{\mathrm{Ox}}/\mathrm{Ti}_{\mathrm{rate}}$	Phase	Transport
A	25	1.2×10^{13}	3×10^{-7}	2.9	cr-$\mathrm{Ti_2O_3}$	I
B	25	1.2×10^{13}	4×10^{-8}	0.4	c-$\mathrm{TiO}_{1-\delta}$, γ-$\mathrm{Ti_3O_5}$	M
C	25	1.2×10^{13}	8×10^{-8}	0.8	c-$\mathrm{TiO}_{1-\delta}$, γ-$\mathrm{Ti_3O_5}$	M
D	45	2.4×10^{13}	2×10^{-7}	1.0	c-$\mathrm{TiO}_{1-\delta}$, γ-$\mathrm{Ti_3O_5}$	M, SC
E	85	2.4×10^{13}	2×10^{-7}	1.0	c-TiO, γ-$\mathrm{Ti_3O_5}$	I, SC
F	80	1.7×10^{13}	2×10^{-7}	1.4	c-TiO/γ-$\mathrm{Ti_3O_5}$, cr-$\mathrm{Ti_2O_3}$, $\mathrm{Ti_4O_7}$	I, SC

field H applied parallel to the sample surface. Figure 3(b) shows the suppression of T_c for $0 < H < 7$ T. The upper critical field $H_{C2}(T)$ is defined by a 90% drop in the normal state resistance. Figure 3(c) shows a plot of H_{C2} as a function of temperature. The results are fit to the Werthamer-Helfand-Hohenberg equation $H_{C2}(T) = H_{C2}(0)[1 - (\frac{T}{T_C})^2]$ [24]. From the fit, the upper critical field at 0 K $H_{C2}(0)$ is determined to be 9.8 T. The coherence length ξ is determined to be 5.7 nm from the Ginzburg-Landau superconducting coherence length relation, $\xi = \{(\hbar/2e)/[H_{c2}(0)]\}^{1/2}$. The measured coherence length is comparable to previous reports [6,16].

The insulating-superconducting transition was previously observed in $\mathrm{Ti}_x\mathrm{O}_y$ films [3,14] and another three-dimensional superconductor, $\mathrm{BaPb}_{1-x}\mathrm{Bi}_x\mathrm{O}_3$, which also exhibits a strong dependence of T_c on the film thickness and the presence of multiple polymorphs (tetragonal and orthorhombic fractions of $\mathrm{BaPb}_{1-x}\mathrm{Bi}_x\mathrm{O}_3$) [25]. Thus, structural disorder arising from local fluctuations in oxygen content may enhance disorder leading to the insulator-superconductor transition.

B. XRD structure

The relationship between the synthesis conditions, crystal structure, and the transport properties is determined by synchrotron XRD measurements at the 33-ID beamline at the Advanced Photon Source. Figure 4(a) shows a specular scan around the substrate (0006) Bragg peak measured with an x-ray energy of 16 KeV ($\lambda = 0.774$ Å) for a series of $\mathrm{Ti}_x\mathrm{O}_y$ samples. For sample A, grown with the highest $P_{\mathrm{Ox}}/\mathrm{Ti}_{\mathrm{rate}}$ ratio, the main Bragg peak corresponds to the cr-$\mathrm{Ti_2O_3}$ phase. A second peak corresponding to a slightly O-rich c-TiO layer is observed.

The diffraction intensities for the 25 nm metallic $\mathrm{Ti}_x\mathrm{O}_y$ film (sample B) comprise a broad shoulder with lattice spacing $d = 2.423$ Å and a main peak with $d = 2.375$ Å. The shoulder and main peaks correspond, respectively, to the (111) Bragg reflection of oxygen-deficient c-$\mathrm{TiO}_{-\delta}$ and the (022) Bragg peak of γ-$\mathrm{Ti_3O_5}$ compressively strained to the buffer layer.

While weak insulating behavior has been reported for c-$\mathrm{TiO}_{1+\delta}$, the observation of metallicity in samples B and C arises from the stabilization of Ti-rich/oxygen-poor c-$\mathrm{TiO}_{1-\delta}$ due to the low growth oxygen pressures. For $0.05 \leqslant \delta \leqslant 0.2$, Hulm *et al.* showed metallicity for as-cast single-phase c-$\mathrm{TiO}_{1-\delta}$ samples [3]. An expansion in the lattice parameter is expected for the oxygen-deficient c-$\mathrm{TiO}_{1-\delta}$ [3]; hence, from fits to the 00L data, the broad shoulder at low L ($c_{\mathrm{measured}} = 4.19$ Å) is assigned to an ~15 Å thick metallic c-$\mathrm{TiO}_{1-\delta}$ layer which dominates the resistivity measurements in Fig. 3(a). Annealing sample B in flowing $\mathrm{O_2}$ for 3 h at 600 °C leads to the oxidation of both layers and a shift in the Bragg peaks to $d = 2.324$ Å corresponding to the formation of cr-$\mathrm{Ti_2O_3}$ and a metal-insulator transition.

The 45 nm metallic sample D also has a main peak at $d = 2.385$ Å corresponding to the (022) peak of γ-$\mathrm{Ti_3O_5}$ and a shoulder with $d = 2.4171$ Å corresponding to slightly oxygen-deficient c-$\mathrm{TiO}_{1-\delta}$. The metallicity observed for this sample is again due to the metallic oxygen-deficient c-$\mathrm{TiO}_{1-\delta}$ layer. Around 3.7 K, a decrease in the resistivity is observed [Fig. 3(a), inset] due to the superconducting transition in the γ-$\mathrm{Ti_3O_5}$ layer [18].

The superconducting sample E has a main Bragg peak at $d = 2.388$ Å corresponding to the (022) peak of relaxed γ-$\mathrm{Ti_3O_5}$. Close to the (044) γ-$\mathrm{Ti_3O_5}$ in Fig. 4(b), we observe a shoulder at lower q which corresponds to the (222) reflection of cubic stoichiometric TiO ($c_{\mathrm{measured}} = 4.167$ Å). The metallic phase is strongly suppressed, possibly due to the longer deposition time, which allows for complete oxidation of the c-TiO buffer layer. The transport properties of sample

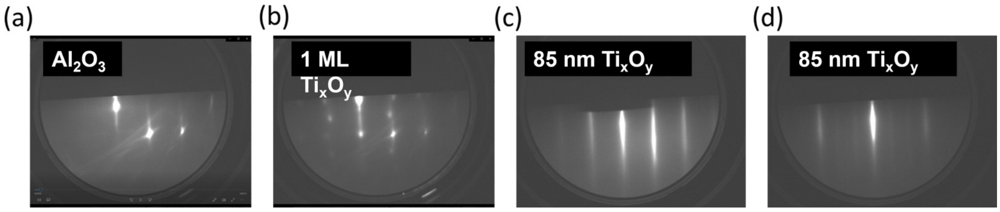

FIG. 2. Evolution of the surface RHEED pattern for the growth of the 85 nm thick $\mathrm{Ti}_x\mathrm{O}_y$ film on (0001)-oriented α-$\mathrm{Al_2O_3}$ at $P_{\mathrm{O2}} = 2 \times 10^{-7}$ Torr and a growth rate of 2.5 Å/min (sample E). Diffraction pattern of (a) the initial $\mathrm{Al_2O_3}$ surface and (b) after 1 ML $\mathrm{Ti}_x\mathrm{O}_y$ along the $[11\bar{2}0]$ azimuth and after 85 nm along (c) the $[11\bar{2}0]$ and (d) $[10\bar{1}0]$ directions.

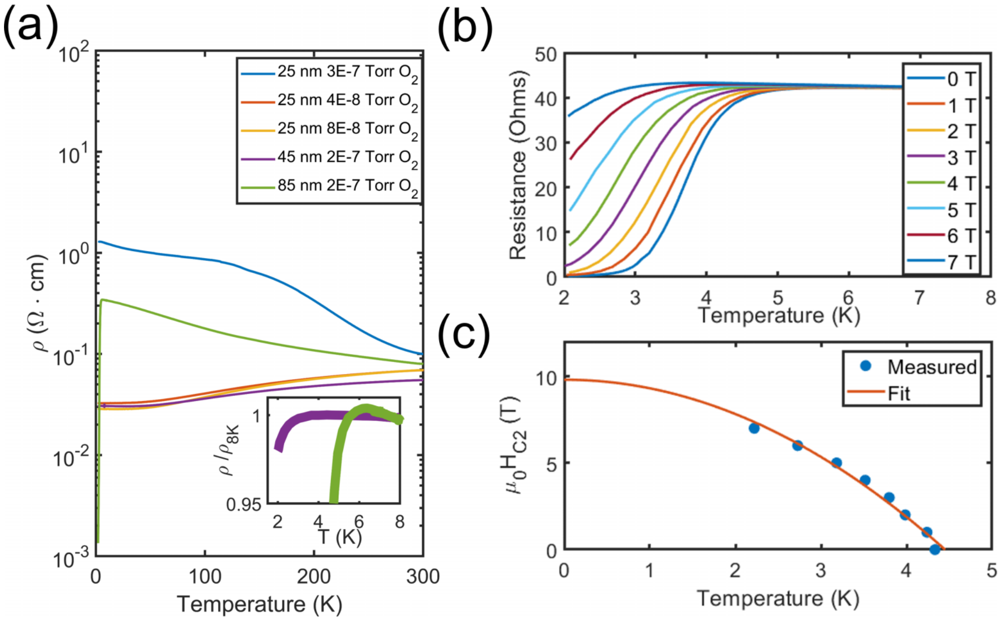

FIG. 3. (a) Comparison of sheet resistance for MBE-grown Ti_xO_y films as a function of growth oxygen pressure and film thickness. The inset shows the drop in resistivity at low temperatures for the superconducting samples (samples D and E). (b) Resistivity as a function of magnetic field applied in plane for the 85 nm thick Ti_xO_y film (sample E) grown at $P_{\mathrm{Ox}} = 2 \times 10^{-7}$ Torr. (c) Relationship between critical magnetic field and T_c and the corresponding Werthamer-Helfand-Hohenberg fit.

E in Fig. 3(a) are dominated by the superconducting relaxed γ-Ti_3O_5 phase [17].

Based on the x-ray diffraction measurements, the emergent picture of the structural profiles of the films under different growth conditions is summarized in Fig. 5. Oxygen-poor growth of Ti_xO_y on (0001)-oriented α-Al_2O_3 at high growth temperatures leads to the formation of a thin (111)-oriented cubic $TiO_{1-\delta}$ metallic buffer layer. As the film thickness increases, if the oxygen pressure is sufficiently high, the structure transforms into the Magnéli γ-Ti_3O_5 phase. γ-Ti_3O_5 is initially strained to the buffer layer, and the strain is relaxed as the film thickness is increased. Since pressure is known to suppress superconductivity in Ti_xO_y [6], this picture is consistent with the observed increase in T_c with increasing film thickness [15,17].

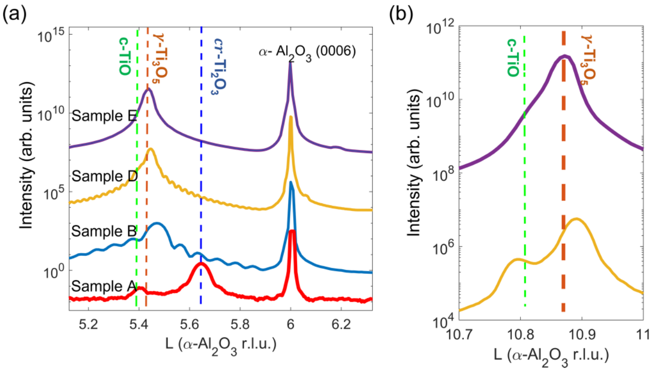

FIG. 4. (a) Comparison of specular x-ray diffraction around the α-Al_2O_3 (0006) Bragg peak for sample A (25 nm, $P_{\mathrm{Ox}} = 3 \times 10^{-7}$ Torr), B (25 nm, $P_{\mathrm{Ox}} = 4 \times 10^{-8}$ Torr), D (45 nm, $P_{\mathrm{Ox}} = 2 \times 10^{-7}$ Torr), and E (85 nm, $P_{\mathrm{Ox}} = 2 \times 10^{-7}$ Torr) Ti_xO_y films grown by MBE. (b) Corresponding reflections for samples D and E at higher q.

C. Phase segregation in Ti_xO_y

The transport and structural results indicate a strong correlation between the growth conditions and film thickness on the physical and structural properties of the Ti_xO_y films. Stoichiometric c-TiO has an NaCl structure with lattice constant $c = 4.177$ Å. The NaCl structure is stable for oxygen concentrations ranging from 0.8 to 1.3 with T_c increasing from 0.5 to 1 K for bulk c-TiO_x [3,5,8,26]. The tendency of Ti_xO_y to form Magnéli phases and related polymorphs of the form Ti_nO_{2n-1} suggests that the oxygen stoichiometry and the growth conditions strongly influence the structure and physical properties of the thin films.

To further investigate the delicate balance between film stoichiometry and the transport properties of the Ti_xO_y system, we consider the structural properties of a eutectic film formed by growing it at a reduced Ti rate with an oxygen pressure of 2×10^{-7} Torr. The slight increase in the O/Ti

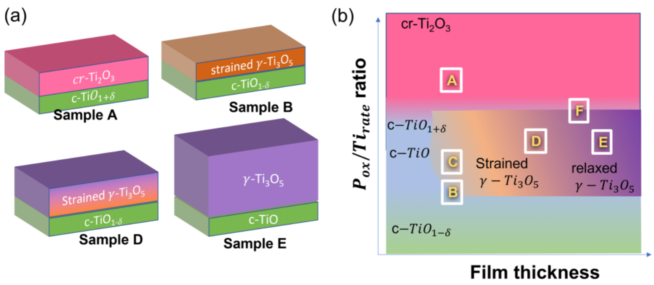

FIG. 5. (a) Schematic structures of samples A, B, D, and E determined from x-ray diffraction measurements and (b) the corresponding phase diagram showing the relationship between the ratio of the growth oxygen pressure P_{Ox} to the Ti flux rate and the film thickness.

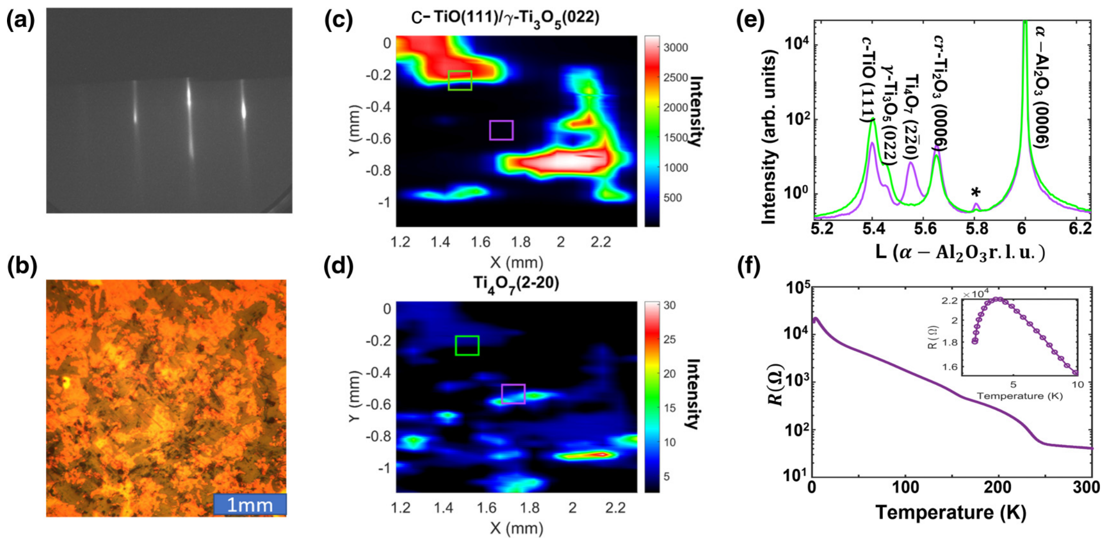

FIG. 6. Structural and transport properties of an 80 nm thick Ti_xO_y film grown at a Ti flux rate of 1.8 Å/min in $P_{O2} = 2 \times 10^{-7}$ Torr (sample F). (a) Reflection high-energy diffraction for 80 nm Ti_xO_y on (0001)-oriented Al_2O_3. (b) Optical micrograph of the film indicating structural domains. High-resolution synchrotron x-ray diffraction raster maps around Bragg peaks observed at diffraction conditions fixed for (c) the c-TiO (111) Bragg peak and (d) the Ti_4O_7 $(2\bar{2}0)$ Bragg peak indicating structural phase separation. (e) Specular diffraction along the substrate $00L$ direction at different points on the sample. (f) Resistance versus temperature. The inset shows the superconducting transition at low temperature.

ratio is expected to allow for the thermodynamic stabilization of oxygen-rich Ti_xO_y phases such as cr-Ti_2O_3.

The initial RHEED images for the sample grown at the lower Ti rate shows diffraction spots indicative of surface roughening; however, the final RHEED image in Fig. 6(a) shows well-defined 2D streaks after a growth of 80 nm. Figure 6(b) shows an optical image of the as-grown film. Clear dark and "bright" regions are observed, indicating macroscopic phase separation. These variations are not observed for the uniform films previously discussed (Fig. S3 in the Supplemental Material) [23]. To determine the differences in the structure of the observed phases, we perform microdiffraction experiments at the Advanced Photon Source, where the x-ray beam is focused to a 20×40 μm^2 spot size using a Kirkpatrick-Baez mirror. Figures 6(c) and 6(d) show diffraction intensity maps with the diffraction conditions fixed at the c-TiO (111) Bragg reflection and the Ti_4O_7 (2−20) reflection. The maps show that the two phases are not uniformly distributed throughout the sample. Figure 6(e) shows $(00L)$ scans at locations close to the c-TiO phase and the Ti_4O_7 domain. The scans show that the intensity of the Ti_4O_7 is suppressed in regions of the film with increased fractions of the c-TiO and γ-Ti_3O_5 phase. At both locations surveyed in Fig. 6(e), a cr-Ti_2O_3 peak is present, indicating that the c-TiO/γ-Ti_3O_5 and Ti_4O_7 grains are located in a matrix of the insulating cr-Ti_2O_3 phase [the regions with zero intensity in Figs. 6(c) and 6(d)]. The Ti_4O_7 grains have lateral dimensions on the order of 100 μm, while the c-TiO/γ-Ti_3O_5 grains are an order of magnitude larger in dimensions. An additional peak indicated by the asterisk (*) at $L \approx 5.8$ reciprocal lattice units ($d = 2.18$ Å) suggests the presence of a small fraction of rutile TiO_2.

The transport properties of the eutectic sample are shown in Fig. 6(f). The multiple electronic transitions are consistent with the coexistence of multiple structural phases. Transitions in the resistivity are observed at 250 and 150 K which are consistent with reported transitions for cr-Ti_2O_3 [19] and Ti_4O_7 [18]. The resistivity drop at 3 K is indicative of a superconducting transition expected for either Ti_4O_7 or γ-Ti_3O_5; however, no zero-resistance state is observed at the instrument's minimum temperature of 2 K.

III. CONCLUSION

In conclusion, we have used a combination of high-resolution synchrotron x-ray diffraction mapping and temperature-dependent transport to investigate the correlation between film thickness, phase separation, and superconductivity in Ti_xO_y films grown on (0001)-oriented α-Al_2O_3. The films with thicknesses ranging from 25 to 85 nm were grown by MBE, where the oxygen stoichiometry of the films is tuned by the oxygen partial pressure and the Ti flux rate during growth. The transport properties were correlated with the P_{Ox}/Ti_{rate} ratio and thickness-dependent strain relaxation. A metallic c-$TiO_{1-\delta}$ buffer layer is formed for films grown under oxygen-poor conditions. A superconducting Magnélli γ-Ti_3O_5 layer nucleates on the buffer layer. Strain relaxation occurs as the film thickness increases and correlates with a thickness-dependent increase in T_c. As the P_{Ox}/Ti flux ratio increases, the buffer composition transitions to an insulating cr-Ti_2O_3 phase. A mixed-phase structure is formed for P_{Ox}/Ti flux ratios close to the c-TiO/cr-Ti_2O_3 phase boundary. These results suggest that the thickness dependence of T_c in Ti_xO_y is related to a complex interplay between strain and the nucleation kinetics of Ti_xO_y phases and polymorphs. Thus, a complete elucidation of phase formation and phase separation and the electronic and structural interactions at interphase boundaries will allow for understanding and enhancing T_c in atomically thin Ti_xO_y layers.

The data that support the findings of this study are available from the corresponding author upon request.

ACKNOWLEDGMENTS

The authors acknowledge financial support from the U.S. National Science Foundation under Grant No. NSF DMR-1751455. V.A.S. was supported by the U.S. Department of Energy, Office of Science, Basic Energy Sciences, under Award No. DE-SC-0012375. This work was performed in part at the Analytical Instrumentation Facility (AIF) at North Carolina State University, which is supported by the state of North Carolina and the National Science Foundation (Award No. ECCS-2025064). This work made use of instrumentation at AIF acquired with support from the National Science Foundation (Grant No. DMR-1726294). AIF is a member of the North Carolina Research Triangle Nanotechnology Network (RTNN), a site in the National Nanotechnology Coordinated Infrastructure (NNCI). Use of the Advanced Photon Source was supported by the U.S. Department of Energy, Office of Science, Office of Basic Energy Sciences, under Contract No. DE-AC02-06CH11357.

[1] N. Doyle, J. Hulm, C. Jones, R. Miller, and A. Taylor, Vacancies and superconductivity in titanium monoxide, Phys. Lett. A **26**, 604 (1968).

[2] H. Iwasaki, N. F. Bright, and J. Rowland, The polymorphism of the oxide Ti_3O_5, J. Less-Common Met. **17**, 99 (1969).

[3] J. Hulm, C. Jones, R. Hein, and J. Gibson, Superconductivity in the TiO and NbO systems, J. Low Temp. Phys. **7**, 291 (1972).

[4] D. S. McLachlan, New models for the positive and negative temperature coefficients of resistivity for $TiO_{0.80-1.23}$ metallic oxides, Phys. Rev. B **25**, 2285 (1982).

[5] T. Reed, M. Banus, M. Sjöstrand, and P. Keesom, Superconductivity in cubic and monoclinic "TiO," J. Appl. Phys. **43**, 2478 (1972).

[6] C. Zhang, F. Hao, G. Gao, X. Liu, C. Ma, Y. Lin, Y. Yin, and X. Li, Enhanced superconductivity in TiO epitaxial thin films, npj Quantum Mater. **2**, 2 (2017).

[7] T. Wagner and M. Agarwal, Growth and structure of Ti_2O_3 and TiO_2 thin films on (0001) α-$A1_2O_3$ substrates, MRS Proc. **472**, 81 (1997).

[8] F. Li, Y. Zou, M.-G. Han, K. Foyevtsova, H. Shin, S. Lee, C. Liu, K. Shin, S. D. Albright, R. Sutarto, F. He, B.A. Davidson, F. J. Walker, C. H. Ahn, Y. Zhu, Z. G. Cheng, I. Elfimov, G. A. Sawatzky, and K. Zou, Single-crystalline epitaxial TiO film A metal and superconductor, similar to Ti metal, Sci. Adv. **7**, eabd4248 (2021).

[9] K. B. Alexander, F. J. Walker, R. A. McKee, and F. A. List III, TiO_x/Al_2O_3 multilayer ceramic thin films, J. Am. Ceram. Soc. **73**, 1737 (1990).

[10] Y. Li, Z. G. Yu, L. Wang, Y. Weng, C. S. Tang, X. Yin, K. Han, H. Wu, X. Yu, L. M. Wong, D. Wan, Xiao R. Wang, J. Chai, Y.-W. Zhang, S. Wang, J. Wang, A. T. S. Wee, M. B. H. Breese, S. J. Pennycook, T. Venkatesan, S. Dong, J. M. Xue, and J. Chen, Electronic-reconstruction enhanced hydrogen evolution catalysis in oxide polymorphs, Nat. Commun., Nat. Commun. **10**, 3149 (2019).

[11] Y. Li, Y. Weng, X. Yin, X. Yu, S. S. Kumar, N. Wehbe, H. Wu, H. N. Alshareef, S. J. Pennycook, M. B. Breese, J. Chen, S. Dong, and T. Wu, Orthorhombic Ti_2O_3: A polymorph-dependent narrow-bandgap ferromagnetic oxide, Adv. Funct. Mater. **28**, 1705657 (2018).

[12] K. Yoshimatsu, N. Hasegawa, Y. Nambu, Y. Ishii, Y. Wakabayashi, and H. Kumigashira, Metallic ground states of undoped Ti_2O_3 films induced by elongated c-axis lattice constant, Sci. Rep. **10**, 22109 (2020).

[13] J. Xu, D. Wang, H. Yao, K. Bu, J. Pan, J. He, F. Xu, Z. Hong, X. Chen, and F. Huang, Nano titanium monoxide crystals and unusual superconductivity at 11 K, Adv. Mater. **30**, 1706240 (2018).

[14] C. Zhang, Y. Fan, Q. Chen, T. Wang, X. Liu, Q. Li, Y. Yin, and X. Li, Quantum Griffiths singularities in TiO superconducting thin films with insulating normal states, npg Asia Mater. **11**, 76 (2019).

[15] Y. Li, Y. Weng, J. Zhang, J. Ding, Y. Zhu, Q. Wang, Y. Yang, Y. Cheng, Q. Zhang, P. Li, J. Lin, W. Chen, Y. Han, X. Zhang, L. Chen, X. Chen, J. Chen, S. Dong, X. Chen and T. Wu, Observation of superconductivity in structure-selected Ti_2O_3 thin films, npg Asia Mater. **10**, 522 (2018).

[16] Y. J. Fan, C. Ma, T. Y. Wang, C. Zhang, Q. L. Chen, X. Liu, Z. Q. Wang, Q. Li, Y. W. Yin, and X. G. Li, Quantum superconductor-insulator transition in titanium monoxide thin films with a wide range of oxygen contents, Phys. Rev. B **98**, 064501 (2018).

[17] Y. Fan, C. Zhang, X. Liu, Y. Lin, G. Gao, C. Ma, Y. Yin, and X. Li, Structure and transport properties of titanium oxide (Ti_2O, $TiO_{1+\delta}$, and Ti_3O_5) thin films, J. Alloys Compd. **786**, 607 (2019).

[18] K. Yoshimatsu, O. Sakata, and A. Ohtomo, Superconductivity in Ti_4O_7 and γ-Ti_3O_5 films, Sci. Rep. **7**, 12544 (2017).

[19] H. Kurokawa, K. Yoshimatsu, O. Sakata, and A. Ohtomo, Effects of phase fraction on superconductivity of low-valence eutectic titanate films, J. Appl. Phys. **122**, 055302 (2017).

[20] K. Yoshimatsu, H. Kurokawa, K. Horiba, H. Kumigashira, and A. Ohtomo, Large anisotropy in conductivity of Ti_2O_3 films, APL Mater. **6**, 101101 (2018).

[21] C. Zhang, F. Hao, X. Liu, Y. Fan, T. Wang, Y. Yin, and X. Li, Quasi-two-dimensional vortex–glass transition and the critical current density in TiO epitaxial thin films, Supercond. Sci. Technol. **31**, 015016 (2018).

[22] D. Wang, C. Huang, J. He, X. Che, H. Zhang, and F. Huang, Enhanced superconductivity in rock-salt TiO, ACS Omega **2**, 1036 (2017).

[23] See Supplemental Material at http://link.aps.org/supplemental/10.1103/PhysRevMaterials.6.064805 for additional in-situ reflection high energy electron diffraction, atomic force microscopy, and optical microscope measurements.

[24] N. Werthamer, E. Helfand, and P. Hohenberg, Temperature and purity dependence of the superconducting critical field, H_{c2}. III. Electron spin and spin-orbit effects, Phys. Rev. **147**, 295 (1966).

[25] D. T. Harris, N. Campbell, R. Uecker, M. Brützam, D. G. Schlom, A. Levchenko, M. S. Rzchowski, and C.-B. Eom, Superconductivity-localization interplay and fluctuation magnetoresistance in epitaxial $\mathrm{BaPb}_{1-x}\mathrm{Bi}_x\mathrm{O}_3$ thin films, Phys. Rev. Materials **2**, 041801(R) (2018).

[26] M. Banus, T. Reed, and A. Strauss, Electrical and magnetic properties of TiO and VO, Phys. Rev. B **5**, 2775 (1972).

Correction: The previously published Figure 3 contained incorrect axis labeling along the ordinate of part (c) and has been replaced.